SHocks: structure, AcceleRation, dissiPation

Work Package 3
Particle energization and dissipation processes at shocks

Deliverable D3.4
Electron dynamics, heating, and acceleration

Prepared by: Michael Gedalin
on behalf of SHARP

This project has received funding from the European Union's Horizon 2020 research and innovation programme under grant agreement No 101004131

Document Change Record

Issue	Date	Author	Details
1.0	9.12.2023	Gedalin	First version
1.1	19.12.2023	Gedalin	Final version

Table of Contents

1 Summary

Electron heating and acceleration in collisionless shocks is a long standing problem. Rapid isotropization of heated electrons cannot be explained solely by the cross-shock potential, which is also prevents efficient reflection and injection into the diffusive acceleration regime. Recent observations have shown that small-scale electric fields are present in the shock front, together with the large-scale cross-shock potential. These small-scale fields have been found also in the upstream and downstream regions. Electron heating in shocks is produced by combined action of the large- and small-scale fields, when the large scale potential determines the energy transferred to the electrons while scattering small-scale fields causes efficient diffusion in the velocity space. Electron reflection is substantially enhanced in the presence of small-scale fields. Scattering on these fields apparently replaces negligible Coulomb collisions with efficient turbulent collisions. Small-scale electric spikes may also affect electron dynamics in the upstream and downstream region, providing scattering, including reflection, at low energies, thus starting electron injection.

2 Introduction

Collisionless shocks are one of the most ubiquitous nonlinear systems in space plasmas. When viewed in the shock frame, the energy of the directed plasma flow is redistributed to heating of the bulk of ions and electrons and acceleration of a small number of charged particles to high energies. In fast magnetosonic shocks magnetic field enhancement also takes a part of the energy budget. Most of the energy goes into ion heating. The mechanism of ion heating is rather well understood [see, e.g. Gedalin, 2019, and references therein]. Electron heating is substantially weaker and in strong shocks may constitute less than 10% of the ion heating [Schwartz et al., 1988, Ghavamian et al., 2013, Gedalin et al., 2023]. Yet, knowledge of the amount of electron heating and of the physical mechanism of the formation of the heated electron distribution is crucial for understanding of the physics of the remote astrophysical shocks, where heated and accelerated electrons are responsible for the most of the observed electromagnetic radiation [Reynolds and Keohane, 1999, Laming, 2000, Helder et al., 2011, Vink, 2012, Ghavamian et al., 2013, Vink et al., 2015]. Heliospheric observations allow us to study the mechanisms of electron heating and acceleration with in situ measurements.

Before the 1980s, it was thought that electrons are heated by the turbulence within the shock front. Adiabatic magnetic compression (conservation of the magnetic moment) alone would result in perpendicular heating at the expense of the parallel degree of freedom. Here perpendicular and parallel refer to the direction of the local magnetic field. Transfer of energy from ions requires existence of the cross-shock potential which decelerates ions and accelerates electrons across the shock. Let x be the coordinate along the shock normal of a planar shock, for simplicity. In what follows we shall frequently refer to two shock frames. The normal incidence frame (NIF) is the shock frame in which the upstream plasma flow is along the shock normal. The de Hoffman-Teller frame (HT) is the shock frame in which the upstream plasma flow is along the upstream magnetic field. In any of these the cross-shock potential is $\phi = -\int E_x dx$, where E_x is the electric

field. In HT there is no other macroscopic electric field, so that each proton loses the same energy $e\phi_{HT}$ upon crossing from upstream to downstream, and each electrons gains the same energy. Adiabatic acceleration in a macroscopic cross-shock potential [Goodrich and Scudder, 1984, Scudder et al., 1986b, Thomsen et al., 1987, Schwartz et al., 1988, Hull et al., 2001] would result in acceleration of the bulk of electrons along the magnetic field, while an additional mechanism is required to isotropize the distribution. Liouville mappings in such macroscopis cross-shock field [Scudder et al., 1986a, Hull et al., 2001] should be done in both directions since there is substantial leakage from the heated downstream electron distribution. Unless global demagnetization occurs in a very thin shock, inside the ramp the electron distribution should consist of two counter streaming flows and be strongly unstable. The cross-shock potential issue evolved from Gaussian fit to three points per transition [Scudder et al., 1986b] and ignoring higher resolution measurements [Wygant et al., 1987] to the suspicion that there is no macroscopic cross-shock potential at all, in view of the measurements of the strong small-scale fields. There is no contradiction though. The relation $\phi = -\int E_x dx$ is valid even if E_x consists of a large amplitude field small-scale bursts and a weak mean field slowly varying at the scale of the whole ramp. Direct measurements of the cross-shock potential are difficult [Bale et al., 2002, Balikhin et al., 2002, Walker et al., 2004, Dimmock et al., 2012, Hanson et al., 2019]. Proper integration across the shock requires switching to NIF or HT and is therefore sensitive to the determination of the shock normal and the shock speed. Both prone to substantial errors [Gedalin et al., 2021]. Despite the problems of direct observational determination of the cross-shock potential, its existence is absolutely necessary to transfer energy from ions to electrons and magnetic field. It can be estimated by examination of the ion distributions at the shock front and by careful comparison of theoretical predictions with observations [Pope et al., 2019, Gedalin et al., 2020].

Observations at the Earth bow shock, especially by the Magnetospheric Multiscale (MMS), clearly show that the shock transition is filled with small scale coherent electrostatic structures which can be expected to affect electron heating and, possibly, electron reflection and injection into pre-acceleration regime [Bale et al., 2002, Hull et al., 2006, Hobara et al., 2008, Wilson et al., 2010, 2014, Wilson III et al., 2014, Vasko et al., 2018, Goodrich et al., 2018, Hanson et al., 2019, Wang et al., 2020, Vasko et al., 2020, Wang et al., 2021, 2022].Presence of large-amplitude small-scale electrostatic structures all over the shock lead to suspicion that they alone can decelerate ions [Goodrich et al., 2018]. It was shown, however, that this does not happen [Gedalin, 2020]. Demagnetization of electrons in a strongly inhomogeneous electric field of the shock ramp was predicted by Balikhin et al. [1993]. Demagnetization of electrons in small-scale structures [See et al., 2013, Mozer and Sundkvist, 2013] occurs because the width of the structure is smaller than the electron gyroradius. Recent works revive stochastic interaction of electrons with short scale electrostatic fields as the major player in electron heating [Amano and Hoshino, 2009, Matsumoto et al., 2013, Artemyev et al., 2014, Matsumoto et al., 2015, Artemyev et al., 2017, Katou and Amano, 2019, Tran and Sironi, 2020, Artemyev et al., 2022, Kamaletdinov et al., 2022], focusing on solitary unipolar or bipolar structures, often of Debye size. At present, the two approaches to electron heating are often considered mutually exclusive. Electrons are thought to be heated by either macroscopic cross-shock potential or many small-scale elec-

tric structures. Gedalin [2020] proposed a combined approach taking into account both small-scale electrostatic structures and a large-scale potential. In this approach the integrated cross-shock potential determines the energy transferred to the electrons while the small-scale fields provide scattering in the velocity space to shape the distribution.

Electron acceleration is less studied. Sufficiently high energy electrons may be scattered by the ion-scale turbulence and, therefore, may be accelerated by the diffusive shock acceleration [Jebaraj et al., 2023]. Such relativistic electrons have been detected at the Earth bow shock and interplanetary shocks [Liu et al., 2019, Jebaraj et al., 2023]. The problem is to convert some electrons from the thermal distribution into a superthermal tail which would be able to cross the shock back and forth and gradually gain more energy. This requires electron reflection, as a first step. Reflection by magnetic mirroring in nearly-perpendicular shocks [Leroy and Mangeney, 1984, Wu, 1984], injection by whistlers [see, e.g. Riquelme and Spitkovsky, 2011, and references therein], or pre-acceleration due to trapping and drift in a rippled shock front [see Trotta and Burgess, 2019, and references therein] have been proposed, all for high-Mach number quasi-perpendicular shocks, typically $\theta_{Bn} > 80°$. Here θ_{Bn} is the angle between the shock normal and the upstream magnetic field vector. The Alfvén Mach number is the ratio of the shock speed, that is, the upstream plasma velocity along the shock normal, V_u, to the Alfv'én speed, $v_A = B_u/\sqrt{4\pi n_u m_p}$. Here B_u is the upstream magnetic field magnitude, n_u is the upstream ion number density, and m_p is the proton mass. Low-Mach number or quasi-parallel shocks are supposed to have substantially smaller gradients [Burgess and Scholer, 2013, Krasnoselskikh et al., 2013], required for the mentioned mechanisms. Small-scale electrostatic fields may be able to reflect a part of low-energy electrons, thus starting injection.

3 Detailed account or results

3.1 Small-scale fields: MMS observations

Figure 1 illustrates the fields measured by the MMS at the shock crossing on 2018/11/08 06:37:28 UTC. According to the SHARP database, the shock parameters are: the Alfvénic Mach number $M_A = 3.7$ and the shock angle $\theta_{Bn} = 75°$. The DC magnetic field and magnetic fluctuations are measured separately by different instruments. The DC component is measured by the FluxGate Magnetometer (FGM) at the rate 128 samples/s in the burst mode. The Search-Coil Magnetometer (SCM) measures magnetic waveforms which are provided at the rate 8192 s/s. The Spin-plane Double Probes (SDP) and Axial Double Probes (ADP) provide the electric field vector (EDP) at the rate 8192 s/s with the nominal precision of ~ 1 mV/m. These electric field measurements include the DC component.

Figure 2 shows the fields in a small part of Figure 1. The typical scales of the fluctuations of the FGM DC magnetic field and of the SCM AC magnetic field are similar and much larger than the typical scales of the fluctuations of the EDP electric field.

Figure 3 illustrates the small scale electrostatic activity in the shock front, together with electron heating. For this example, a high-Mach number terrestrial bow shock crossing by MMS1 was chosen rather arbitrarily from the database de-

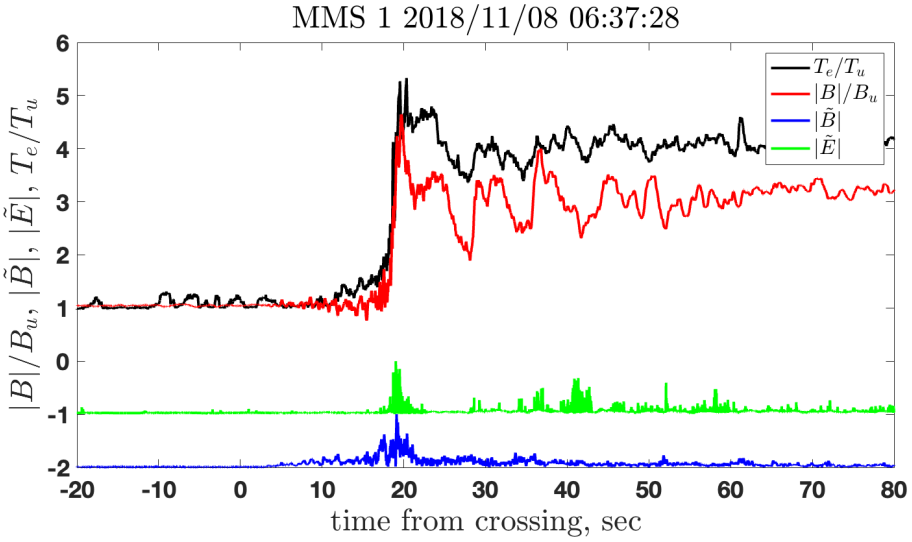

Figure 1: DC and AC fields measured by MMS

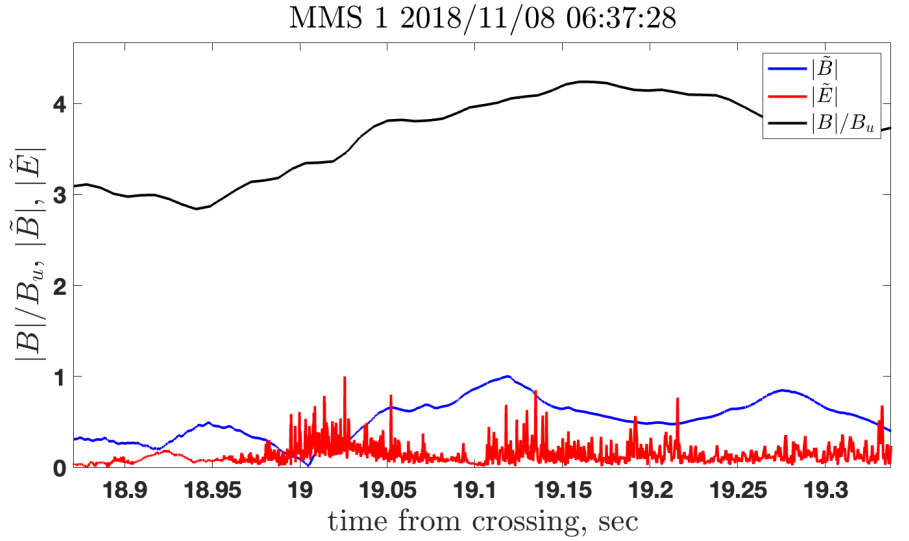

Figure 2: A part of Figure 1.

veloped by the SHARP collaboration [Lalti et al., 2022]. The crossing occurred on 2020/04/22 at 16:44:00. The top left panel is an overview of the shock transition, showing the DC magnetic field magnitude (black, 128 samples/s), the DC electric field magnitude (blue, 8192 samples/s), and the reduced electron distribution function $f(x, v_x)$ (color image, 100/3 samples/s), where x is along the shock normal. The fields are scaled to show in one figure. Other panels show three components of the electric field in various parts of the shock.

Some electric field activity does not seem to have any coherent shape. However, three major coherent shapes were identified: a) a unipolar solitary spike, b) a bipolar spike, and c) a wave packet consisting of nearly monochromatic wave limited by a localized envelope. The first two types have received attention in previous studies [Vasko et al., 2018, Goodrich et al., 2018, Wang et al., 2020, Vasko et al., 2020, Wang et al., 2021, Vasko et al., 2022], while the last type was somehow ignored, although wave packets are very abundant. Figure 4 shows another

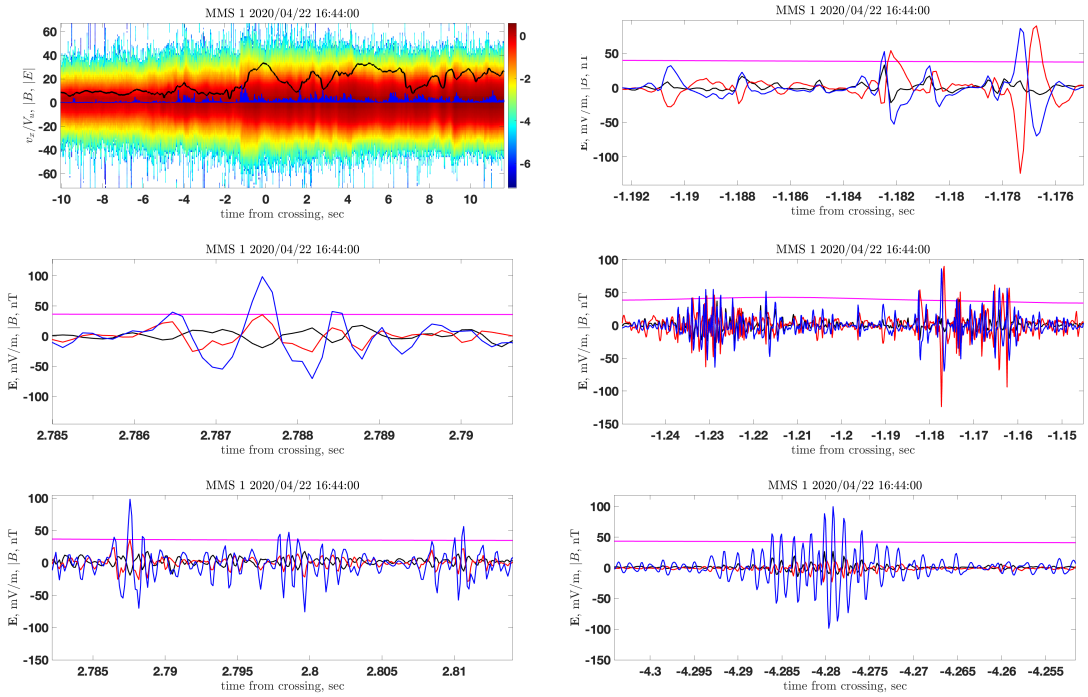

Figure 3: Top left: electron reduced distribution $f(x, v_x)$, magnetic field magnitude (black), and electric field magnitude (blue). Other panels: three components of the electric field in various parts of the shock.

example of the electrostatic activity, together with the electron distribution. Top left panel shows the magnetic field and electron temperature in a moderate-Mach number, M_A, quasi-perpendicular, $\theta_{Bn} = 65°$, terrestrial bow shock crossing by MMS1, chosen rather arbitrarily from the database developed by the SHARP collaboration [Lalti et al., 2022]. The crossing occurred on 2017-11-02 at 08:29:17 UTC. Other panels, except the bottom right, belong to the same crossing. The bottom right panel is for the shock 2020-04-22 at 16:44:00 UTC with $M_A \approx 16$ and $\theta_{Bn} = 55°$. The main shock transition, according to the DC magnetic field, lasts 5 sec, $0 < t < 5$, and the increase of the electron temperature from the upstream value to the maximum occurs there (top left), which means that electron heating is prompt and is determined by the fields there. Top right panel shows that the whole shock transition is covered by a wave train of the AC magnetic field with the period of 1 sec. Middle right panel shows that the electric field bursts are intermittent. A most abundant burst has a shape of a wave packet of the duration of 20-30 ms and a period of 1 ms. Other typical electric waveforms are a unipolar/solitary spike or a bipolar spike, both of 1 ms duration. It has to be noted that conversion of the duration into spatial dependence requires thorough analysis of the wave properties. The magnetic and electric activity presented in Figure 4 has been found in quasi-perpendicular and quasi-parallel shocks as well, from the lowest to highest Mach number shocks in the SHARP database.

3.2 Small-scale features in electron distributions

As an example, another high-Mach number terrestrial bow shock crossing by MMS1 was chosen rather arbitrarily from the database developed by the SHARP

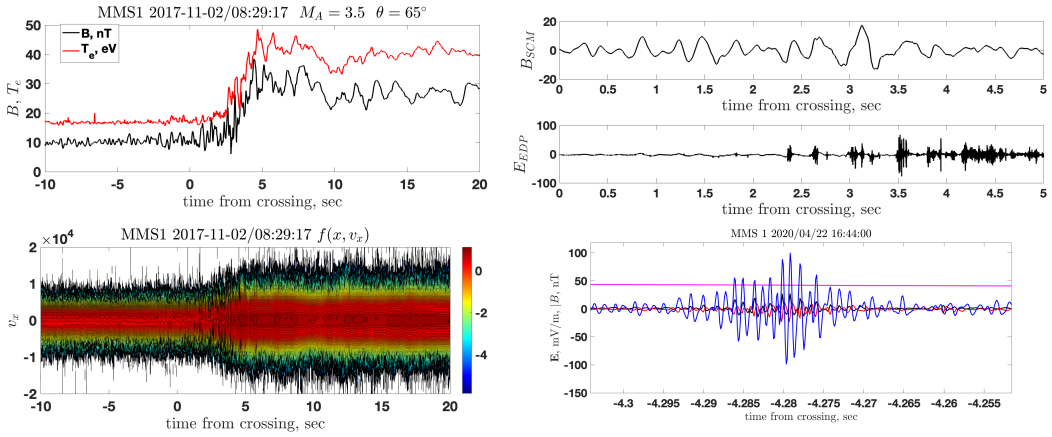

Figure 4: Top left: the magnitude of the DC magnetic field and the electron temperature calculated from FPI burst mode distributions, at 30 ms cadence. Bottom left: the reduced distribution function $f(x, v_x)$ obtained from the same FPI data. Top right: one component of the SCM magnetic field measured at the rate 8192 s/s. Middle right: one component of the EDP electric field measured at the rate 8192 s/s. Bottom right: the most abundant shape of the small-scale electric field.

collaboration [Lalti et al., 2022]. The crossing occurred on 2020/04/22 at 16:44:00. The top left panel is an overview of the shock transition, showing the DC magnetic field magnitude (black, 128 samples/s), the DC electric field magnitude (blue, 8192 samples/s), and the reduced electron distribution function $f(x, v_x)$ (color image, 100/3 samples/s), where x is along the shock normal. The fields are scaled to show in one figure. Figure 5 shows the reduced distribution and the electric field in a small part of the shock. The intermittent electron heating is clearly seen as the

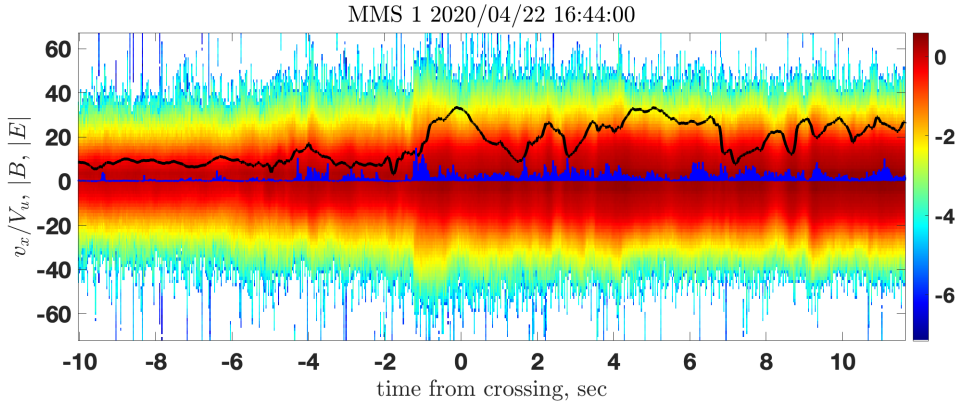

Figure 5: The electron reduced distribution $f(x, v_x)$, the magnetic field magnitude (black) and the electric field magnitude (blue) in a small part of the shock in Figure 3 (top left panel). The velocity v_x and the electric field $|E|$ are scaled to fit the figure.

fluctuating width of the electron distribution. There is no clear visual correlation of the heating pattern with the small-scale electric field pattern. The main broadening of the distribution occurs at the ramp, following the largest magnetic field

increase. In some places broadening seems to coincide with the electric burst but the distribution becomes more narrow again in the subsequent quiet region, which is not consistent with irreversible heating. Careful analysis is required because of the very different time resolution of the field (8192 s/s) and particle measurements (30 ms). All other panels in Figure 3 show the rich variety of the electric field patterns: bipolar structures, short coherent wave packers, long coherent wave packets, and regions combining all of the above mentioned patterns. The spatial distribution of electrostatic activity in shocks is very different: from concentrated almost solely in the ramp to covering a substantial part before the ramp and a large downstream region. Maximum of the electric spikes is not associated either with the sharp magnetic field gradient or with the magnetic maximum or minimum, so that at this stage it is not clear whether there is any relation to the electron current speed. It was suggested that ion-acoustic solitary waves are excited by the bump-on-tail ion instability ("ion holes") [Wang et al., 2022]. Note, however, that these solitary waves last for about 20 ms while the MMS ion distributions are provided at 150 ms cadence, so that the relation is questionable. Electron dynamics in the Debye-scale solitary waves was analyzed in a number of rather similar publications [Artemyev et al., 2014, 2017, Vasko et al., 2018, Kamaletdinov et al., 2022], while other electrostatic structures in the shock front were not given equal attention. Quick analysis of a number of shocks from the SHARP database [Lalti et al., 2022] shows that bursts of wave packets are more typical. Electrons are heated in all shocks which means that heating occurs with all kinds of electrostatic waves.

Test particle analysis of electron dynamics and distributions in a model shock profile, described by Gedalin [2020], has been performed. The electric field, including both the large-scale cross-shock potential and the small-scale spikes, is shown in Figure 6 Figure 7 shows the reduced distribution function $f(x, v_x)$ derived by

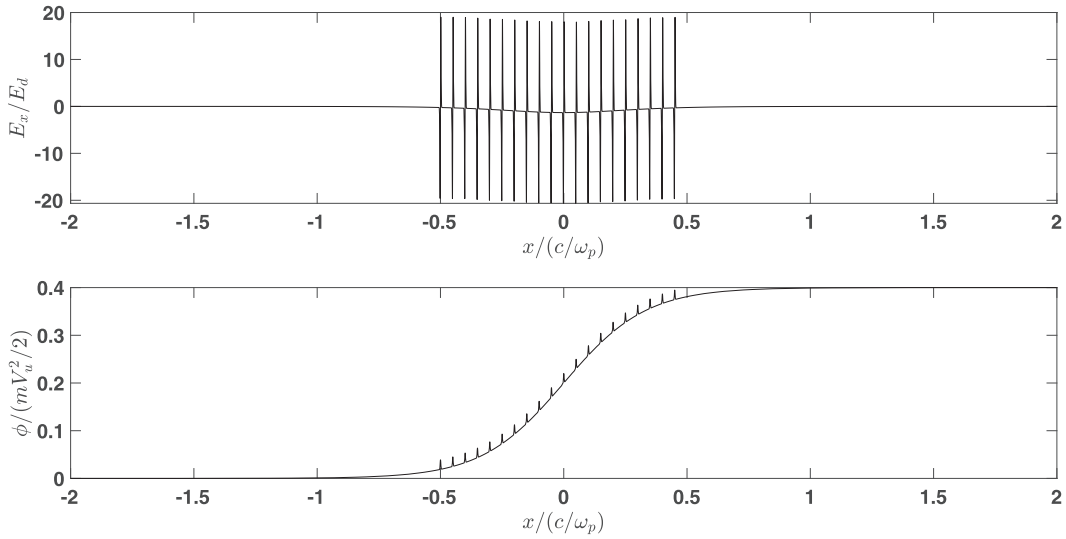

Figure 6: Top: the cross-shock electric field. Bottom: the potential.

tracing electrons in the large-scale field only (top), small-scale field only (middle), and both fields together (bottom). Large-scale field only heats electrons but does not show bursty changes as in Figure 5. Small-scale fields make the changes bursty

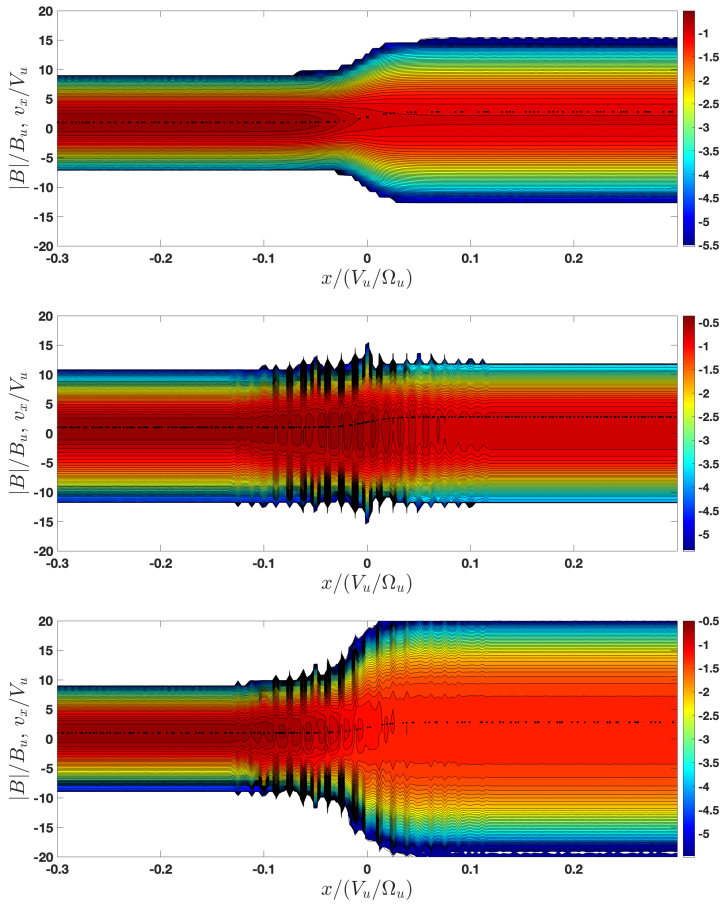

Figure 7: The reduced distribution function $f(x, v_x)$ derived by tracing electrons in the large-scale field only (top), small-scale field only (middle), and both fields together (bottom)

but do not heat. Both fields together provide heating and bursty variations, in agreement with observations.

Figure 8 shows the electron distributions $f(v_\parallel, v_\perp)$ calculated in the de Hoffman-Teller frame far from the shock transition. Here v is the electron speed, $v_\parallel$ is the velocity parallel to the local (upstream or downstream) magnetic field, and $v_\perp = \sqrt{v^2 - v_\parallel^2}$. Electrons with $v_\parallel > 0$ correspond to the downstream distribution. Electrons with $v_\parallel < 0$ are reflected electrons which stream from the shock into the upstream region. The thin blue line separates the two distributions. The initial distribution is Maxwellian. Top left: there is no energization without cross-shock potential while reflection due to the conservation of the magnetic moment is strong. Top right: small-scale structures without a potential greatly enhance reflection but reduce energization of the transmitted electrons. Bottom left: a large-scale potential without small-scale structures accelerates electrons along the magnetic field and suppresses reflection. Bottom right: both electric fields together result in reasonable reflection and energization with substantial perpendicular heating.

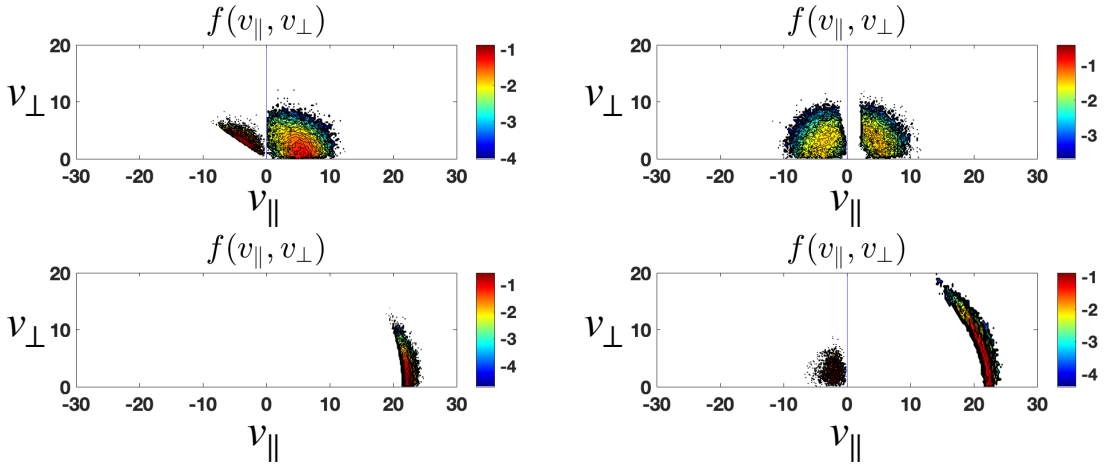

Figure 8: Distribution $f(v_\parallel, v_\perp)$ calculated in the de Hoffman-Teller frame. Top left: no electric field. Top right: only small-scale electric structures. Bottom left: only large-scale cross-shock potential. Bottom right: both large-scale and small-scale electric fields. See details in text.

3.3 Interaction with a single spike

In what follows we perform test particle analysis of electron motion in a single electrostatic spike, in order to answer the following question: how a single spike affects electrons, in particular, whether electrons can be reflected.

The main objective in the analysis of the interaction with a single spike is whether electrons can be reflected. We choose the coordinate x along the shock normal. In what follows we use two shock frames: a) the Normal Incidence Frame (NIF) is the frame in which the upstream plasma flow is along the shock normal, and b) the de Hoffman-Teller frame (HT) is the frame in which the upstream plasma flow is along the upstream magnetic field. The electron thermal gyroradius is

$$\rho_e = \frac{v_{Te}}{\Omega_e} = \frac{m_e}{m_i}\sqrt{\frac{m_i}{m_e}}\frac{v_{Ti}}{\Omega_i} = \sqrt{\frac{m_e}{m_i}}\sqrt{\frac{\beta}{2}}\frac{v_A}{\Omega_i} = \frac{c}{\omega_{pe}}\sqrt{\frac{\beta_e}{2}} \tag{1}$$

where $v_{Te} = \sqrt{T_e/m_e}$ is the electron thermal speed, $\Omega_e = eB/m_e c$ is the electron gyrofrequency, $\omega_{pe} = \sqrt{4\pi n_e e^2/m_e}$ is the electron plasma frequency, B and n are the local magnetic field magnitude and electron number density, and $\beta_e = 8\pi n T_e/B^2$. The spatial scale of a single spike is much smaller than the spatial scale of the magnetic field variation and substantially smaller than the electron inertial length. For the electron tracing we choose the NIF large-scale fields as constants $B_x = B_u \cos\theta_{Bn}$, $B_y = 0$, $B_z = B_u \sin\theta_{Bn}$, $E_y = (V_u B_u/c)\sin\theta_{Bn}$, $E_z = 0$.

In this study three types of the small scale electrostatic field E_x are modeled.

1. A unipolar spike is modeled as a Gaussian

$$E_x = -\frac{\phi}{\sqrt{2\pi}L}\exp\left(-\frac{(x-x_c)^2}{2L^2}\right) \tag{2}$$

of the width L and the center at x_c. The potential across the shape is ϕ.

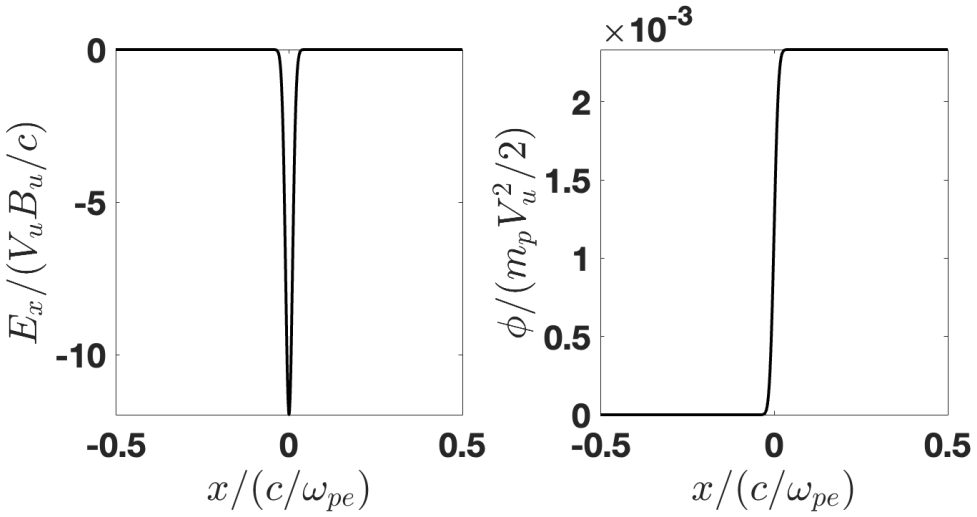

Figure 9: Left panel: the electrostatic field of the bipolar spike used for electron tracing. Right panel: the corresponding cross-spike potential.

2. A bipolar spike is modeled as a difference of Gaussians given by (2). The centers of the Gaussians are shifted, and the amplitudes are of opposite signs. The total cross-spike potential can be controlled using the amplitudes.

3. A wave packet is modeled using the expression

$$E_x = E_0 \cos(2\pi x/W) \exp\left(-\frac{x^2}{2L^2}\right) \tag{3}$$

where the W is the wavelength of the wavetrain and L is the width of the Gaussian envelope.

In all these spikes electrons are demagnetized and their motion is non-adiabatic. We start tracing with incident Maxwellian distribution drifting toward the spike, with the mean velocity $\langle v_x \rangle = V_u$ and β well ahead of the spike (upstream). We follow electrons until they appear well behind the spike (downstream) or well ahead of the spike (backstreaming). The final electron velocities are shifted to HT by adding $v_z^{(HT)} = v_z^{(NIF)} + V_u \tan\theta_{Bn}$. The parallel velocity and the perpendicular speed are calculated as

$$v_\parallel = v_x^{(HT)} \cos\theta_{Bn} + v_z^{(HT)} \sin\theta_{Bn} \tag{4}$$

$$v_\perp = \sqrt{[\boldsymbol{v}^{(HT)}]^2 - v_\parallel^2} \tag{5}$$

and the distributions $f(v_\parallel, f_\perp$ are derived in both regions. These distributions do not depend on at what position the electrons are registered.

We start with a unipolar spike with a small positive cross-spike potential. Figure 9 shows the electrostatic field and the cross-spike potential for the chosen spike The spike parameters are: the width $L = 0.01(c/\omega_{pe})$ and the amplitude corresponding to $2.4 \cdot 10^{-3}(m_pV_u^2/2)$.

Figure 10 shows the electron distributions. There were 5000 electrons in the initial Maxwellian with $\beta = 0.5$, of which 3175 were initially moving toward the spike, of which 115, that is, about 3.5%, are reflected toward the upstream region. The tracing was done for $\theta_{Bn} = 40°$. Figure 11 illustrates the reflection process

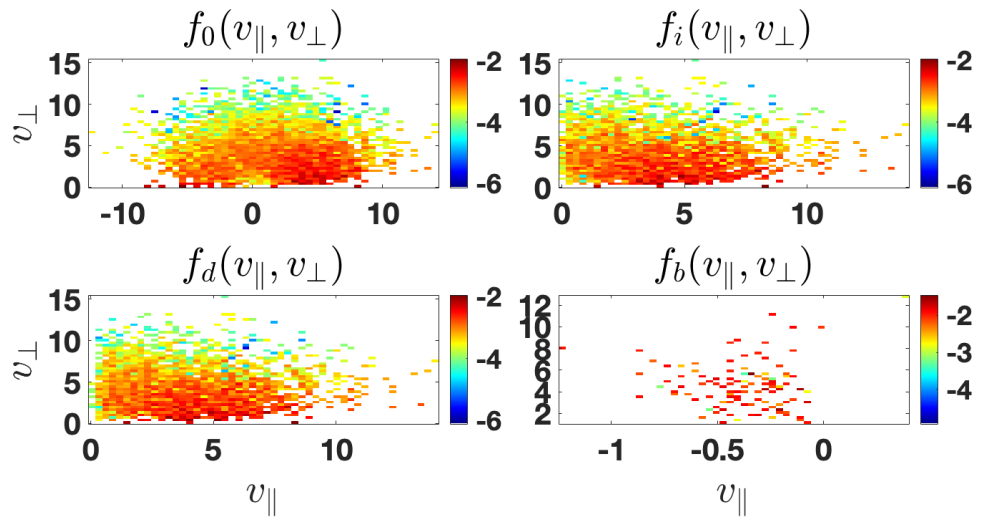

Figure 10: Top left panel: the initial Maxwellian. Top right panel: only the incident electrons moving toward the spike. Left bottom: the electrons crossing the spike and proceeding further downstream. Right bottom: the backstreaming electrons reflected off the spike and proceeding into the upstream region.

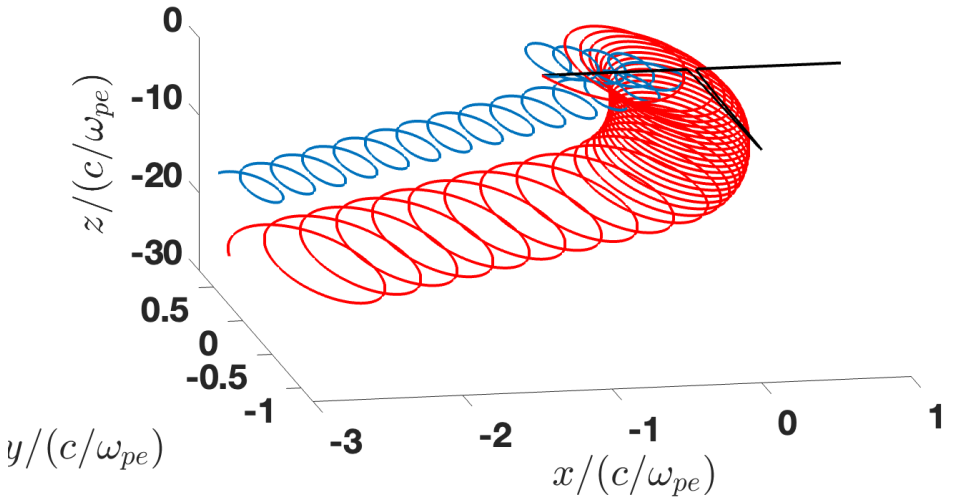

Figure 11: Three-dimensional trajectories of two reflected electrons. The black curve (not to scale) shows the electric field.

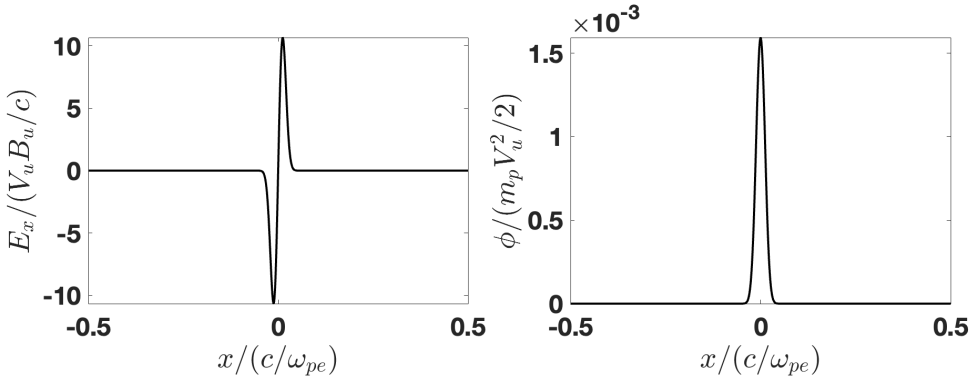

Figure 12: Left panel: the electrostatic field of the bipolar spike used for electron tracing. Right panel: the corresponding cross-spike potential.

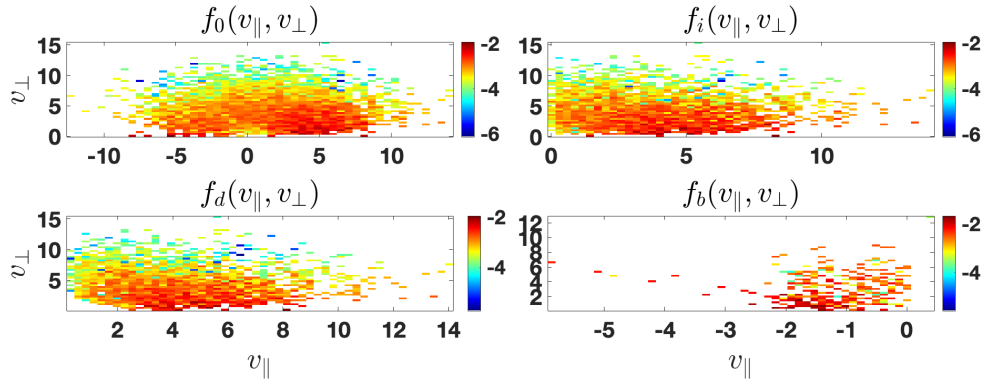

Figure 13: Top left panel: the initial Maxwellian. Top right panel: only the incident electrons moving toward the spike. Left bottom: the electrons crossing the spike and proceeding further downstream. Right bottom: the backstreaming electrons reflected off the spike and proceeding into the upstream region.

by showing 3D trajectories of two reflected electrons. The reflected electrons experience multiple gyrations around the spike before escaping upstream. The electric field inside this spike attracts electrons toward downstream. A spike with a reversed sign of the amplitude, $E_x > 0$, would exert force on electrons toward upstream and is expected to be more efficient in reflection.

Next, we consider a bipolar spike which consists of the previous unipolar spike and its opposite with a shift of $0.02(c/\omega_{pe})$ between the centers. Figure 12 shows the electrostatic field and the cross-spike potential for the chosen bipolar spike The potential reaches its maximum between the Gaussians but the overall potential is zero.The distributions, the number of reflected electrons, and the trajectories of reflected ions do not differ noticeably and are not presented here.

Reversing the polarity of the spike increases the percentage of reflected ions by a factor of two. Figure 13 shows the electron distributions for the reverse spike.

Finally, we analyze the interaction of the same incident electron distribution with the wavepacket shown in Figure 14. The wavelength is $0.04(c/\omega_{pe})$ and the width of the Gaussian envelope is $0.08(c/\omega_{pe})$. The maximum potential is $1.2 \cdot 10^{-3}(m_pV_u^2/2)$. About 15% of the incident electrons are reflected. The corresponding distributions are shown in Figure 15

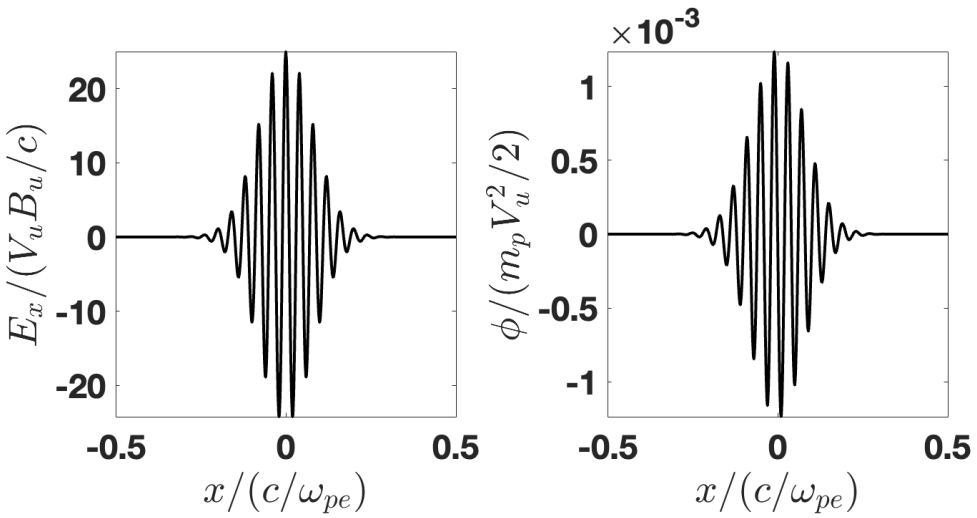

Figure 14: Left panel: the electrostatic field of the wave packet used for electron tracing. Right panel: the corresponding cross-spike potential.

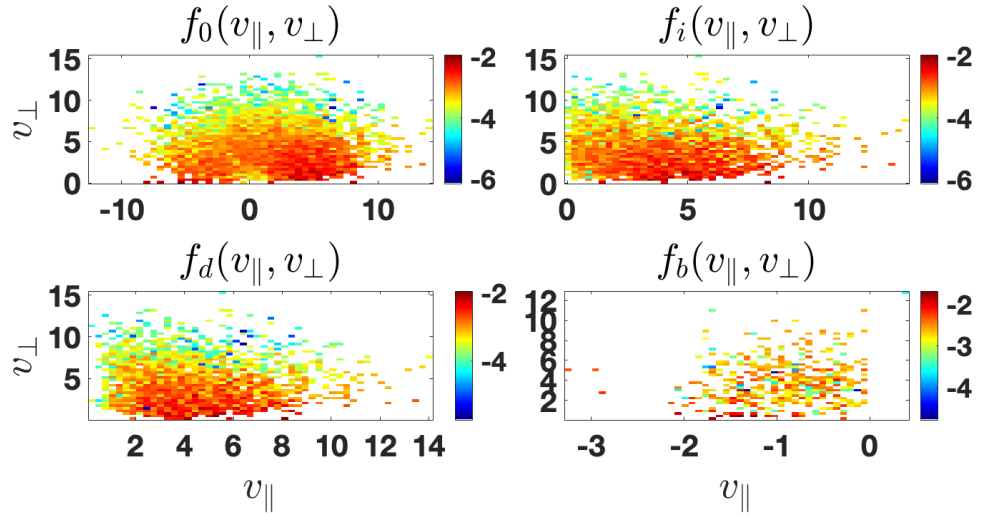

Figure 15: Top left panel: the initial Maxwellian. Top right panel: only the incident electrons moving toward the spike. Left bottom: the electrons crossing the spike and proceeding further downstream. Right bottom: the backstreaming electrons reflected off the spike and proceeding into the upstream region.

In all three types of spikes the maximal potentials are similar. All three are capable of reflecting electrons, the wave packet being the most efficient.

In order to have some understanding of the dependence on the shock angle, electron tracing was performed for the above wave packet and $\theta_{Bn} = 80°$ (about 3% of reflected electrons) and $\theta_{Bn} = 10°$ (about 25% of reflected electrons). Thus, electron reflection occurs at all angles and is more efficient in a quasi-parallel geometry.

4 Conclusions

To summarize, we have found the following:

- The scales of the magnetic and electric fluctuations differ by an order of magnitude at least.
- There are indications of bursty changes of electron distributions within the shock transition.
- The observed electron heating requires presence of the large-scale cross-shock potential and of small-scale electrostatic spikes.
- The downstream electron temperature is determined by the cross-shock potential, isotropization is largely due to the electric spikes
- A single spike is capable of reflecting a part of incident electrons.
- It is suggested that electron reflection off small-scale spikes may provide a mechanism of pre-injection of low energy of electrons into the mechanism of crossing the shock back and forth, as well as providing effective collisions.

5 References

Takanobu Amano and Masahiro Hoshino. Electron Shock Surfing Acceleration in Multidimensions: Two-Dimensional Particle-in-Cell Simulation of Collisionless Perpendicular Shock. *Astrophys. J.*, 690:244, January 2009. doi:10.1088/0004-637X/690/1/244.

A V Artemyev, A A Vasiliev, D Mourenas, O V Agapitov, and V V Krasnoselskikh. Electron scattering and nonlinear trapping by oblique whistler waves: The critical wave intensity for nonlinear effects. *Phys. Plasmas*, 21(10):102903, October 2014. doi:10.1063/1.4897945.

A V Artemyev, R Rankin, and I Y Vasko. Nonlinear Landau resonance with localized wave pulses. *J. Geophys. Res*, 122(5):5519–5527, May 2017. doi:10.1002/2017JA024081.

A. V. Artemyev, X. Shi, T. Z. Liu, X.-J. Zhang, I. Vasko, and V. Angelopoulos. Electron Resonant Interaction With Whistler Waves Around Foreshock Transients and the Bow Shock Behind the Terminator. *J. Geophys. Res*, 127(2), February 2022. ISSN 2169-9380, 2169-9402. doi:10.1029/2021JA029820.

S D Bale, A Hull, D E Larson, R P Lin, L Muschietti, P J Kellogg, K Goetz, and S J Monson. Electrostatic Turbulence and Debye-Scale Structures Associated with Electron Thermalization at Collisionless Shocks. *Astrophys. J.*, 575(1): L25–L28, August 2002. doi:10.1086/342609.

M Balikhin, M Gedalin, and A Petrukovich. New mechanism for electron heating in shocks. *Phys. Rev. Lett.*, 70:1259–1262, March 1993. doi:10.1103/PhysRevLett.70.1259.

M A Balikhin, M Nozdrachev, M Dunlop, V Krasnoselskikh, S N Walker, H St C K Alleyne, V Formisano, M André, A Balogh, A Eriksson, and K Yearby. Observation of the terrestrial bow shock in quasi-electrostatic subshock regime. *J. Geophys. Res.*, 107(A):1155–SSH 1–9, August 2002. doi:10.1029/2001JA000327.

D Burgess and M Scholer. Microphysics of Quasi-parallel Shocks in Collisionless Plasmas. *Space Science Reviews*, 178:513–533, 2013. doi:10.1007/s11214-013-9969-6.

A P Dimmock, M A Balikhin, V V Krasnoselskikh, S N Walker, S D Bale, and Y Hobara. A statistical study of the cross-shock electric potential at low Mach number, quasi-perpendicular bow shock crossings using Cluster data. *J. Geophys. Res*, 117(A):02210, February 2012. doi:10.1029/2011JA017089.

Michael Gedalin. How non-stationary are moderately supercritical shocks? *J. Plasma Phys.*, 85:905850505, 2019. doi:10.1017/S0022377819000692.

Michael Gedalin. Large-scale versus Small-scale Fields in the Shock Front: Effect on the Particle Motion. *Astrophys. J.*, 895(1):0–0, May 2020. doi:10.3847/1538-4357/ab8af0.

Michael Gedalin, Xiaoyan Zhou, Christopher T Russell, and Vassilis Angelopoulos. Overshoot dependence on the cross-shock potential. *Annales Geophysicae*, 38 (1):17–26, January 2020. doi:10.5194/angeo-38-17-2020.

Michael Gedalin, Christopher T. Russell, and Andrew P. Dimmock. Shock Mach Number Estimates Using Incomplete Measurements. *J. Geophys. Res*, 126(10): e2021JA029519, 2021. ISSN 2169-9402. doi:10.1029/2021JA029519.

Michael Gedalin, Michal Golan, Jacco Vink, Natalia Ganushkina, and Michael Balikhin. Electron Heating in Shocks: Statistics and Comparison. *J. Geophys. Res*, 128(9):e2023JA031627, 2023. ISSN 2169-9402. doi:10.1029/2023JA031627.

Parviz Ghavamian, Steven J Schwartz, Jeremy Mitchell, Adam Masters, and J Martin Laming. Electron-Ion Temperature Equilibration in Collisionless Shocks: The Supernova Remnant-Solar Wind Connection. *Space Science Reviews*, 178:633–663, 2013. doi:10.1007/s11214-013-9999-0.

C C Goodrich and J D Scudder. The adiabatic energy change of plasma electrons and the frame dependence of the cross-shock potential at collisionless magnetosonic shock waves. *J. Geophys. Res*, 89:6654–6662, August 1984. doi:10.1029/JA089iA08p06654.

Katherine A Goodrich, Robert Ergun, Steven J Schwartz, Lynn B Wilson, David Newman, Frederick D Wilder, Justin Holmes, Andreas Johlander, James Burch, Roy Torbert, Yuri Khotyaintsev, Per Arne Lindqvist, Robert Strangeway, Christopher Russell, Daniel Gershman, Barbara Giles, and Laila Andersson. MMS Observations of Electrostatic Waves in an Oblique Shock Crossing. *J. Geophys. Res*, 123(1):9430–9442, November 2018. doi:10.1029/2018JA025830.

E L M Hanson, O V Agapitov, F S Mozer, V Krasnoselskikh, S D Bale, L Avanov, Y Khotyaintsev, and B Giles. Cross-Shock Potential in Rippled Versus Planar Quasi-Perpendicular Shocks Observed by MMS. *Geophys. Res. Lett.*, 46(5): 2381–2389, March 2019. doi:10.1029/2018GL080240.

E A Helder, J Vink, and C G Bassa. Temperature Equilibration Behind the Shock Front: An Optical and X-Ray Study Of RCW 86. *The Astrophysical Journal*, 737:85, 2011. doi:10.1088/0004-637X/737/2/85.

Y Hobara, S N Walker, M Balikhin, O A Pokhotelov, M Gedalin, V Krasnoselskikh, M Hayakawa, M André, M Dunlop, H Rème, and A Fazakerley. Cluster observations of electrostatic solitary waves near the Earth's bow shock. *J. Geophys. Res*, 113(A):05211–n/a, May 2008. doi:10.1029/2007JA012789.

A J Hull, J D Scudder, D E Larson, and R Lin. Electron heating and phase space signatures at supercritical, fast mode shocks. *J. Geophys. Res*, 106(A8): 15711–15733, January 2001. doi:10.1029/2001JA900001.

A J Hull, D E Larson, M Wilber, J D Scudder, F S Mozer, C T Russell, and S D Bale. Large-amplitude electrostatic waves associated with magnetic ramp substructure at Earth's bow shock. *Geophysi. Res. Lett.*, 33(15):5987, January 2006. doi:10.1029/2005GL025564.

C. Immanuel Jebaraj, N. Dresing, V. Krasnoselskikh, O. V. Agapitov, J. Gieseler, D. Trotta, N. Wijsen, A. Larosa, A. Kouloumvakos, C. Palmroos, A. Dimmock, A. Kolhoff, P. Kühl, S. Fleth, A. Fedeli, S. Valkila, D. Lario, V. Yu Khotyaintsev, and R. Vainio. Relativistic electron beams accelerated by an interplanetary shock. *Astronomy & Astrophysics*, 2023. ISSN 0004-6361, 1432-0746. doi:10.1051/0004-6361/202348120.

S. R. Kamaletdinov, I. Y. Vasko, A. V. Artemyev, R. Wang, and F. S. Mozer. Quantifying electron scattering by electrostatic solitary waves in the Earth's bow shock. *Physics of Plasmas*, 29(8):082301, August 2022. ISSN 1070-664X, 1089-7674. doi:10.1063/5.0097611.

Takuma Katou and Takanobu Amano. Theory of Stochastic Shock Drift Acceleration for Electrons in the Shock Transition Region. *Astrophys. J.*, 874(2):119, March 2019. ISSN 1538-4357. doi:10.3847/1538-4357/ab0d8a.

V Krasnoselskikh, M Balikhin, S N Walker, S Schwartz, D Sundkvist, V Lobzin, M Gedalin, S D Bale, F Mozer, J Soucek, Y Hobara, and H Comişel. The Dynamic Quasiperpendicular Shock: Cluster Discoveries. *Sp. Sci. Rev.*, 178(2): 535–598, October 2013. doi:10.1007/s11214-013-9972-y.

A. Lalti, Yu. V. Khotyaintsev, A. P. Dimmock, A. Johlander, D. B. Graham, and V. Olshevsky. A Database of MMS Bow Shock Crossings Compiled Using Machine Learning. *J. Geophys. Res*, 127(8), August 2022. ISSN 2169-9380, 2169-9402. doi:10.1029/2022JA030454.

J Laming. Electron Heating at SNR Collisionless Shocks. *Astrophys. J. Suppl. Ser.*, 2000.

M M Leroy and A Mangeney. A theory of energization of solar wind electrons by the earth's bow shock. *Ann. Geophys.*, 2:449–456, 1984.

Terry Z. Liu, Vassilis Angelopoulos, and San Lu. Relativistic electrons generated at Earth's quasi-parallel bow shock. *Science Advances*, 5:eaaw1368, 2019. ISSN 2375-2548. doi:10.1126/sciadv.aaw1368.

Y Matsumoto, T Amano, and M Hoshino. Electron Acceleration in a Nonrelativistic Shock with Very High Alfvén Mach Number. *Phys. Rev. Lett.*, 111(2): 215003, November 2013. doi:10.1103/PhysRevLett.111.215003.

Y Matsumoto, T Amano, T N Kato, and M Hoshino. Stochastic electron acceleration during spontaneous turbulent reconnection in a strong shock wave. *Science*, 347(6):974–978, February 2015. doi:10.1126/science.1260168.

F. S. Mozer and D. Sundkvist. Electron demagnetization and heating in quasiperpendicular shocks. *J. Geophys. Res*, 118(9):5415–5420, September 2013. ISSN 2169-9380, 2169-9402. doi:10.1002/jgra.50534.

S A Pope, M Gedalin, and M A Balikhin. The First Direct Observational Confirmation of Kinematic Collisionless Relaxation in Very Low Mach Number Shocks Near the Earth. *J. Geophys. Res*, 165(1):3–15, March 2019. doi:10.1029/2018JA026223.

S Reynolds and J Keohane. Maximum Energies of Shock-accelerated Electrons in Young Shell Supernova Remnants. *The Astrophysical Journal*, 1999.

Mario A Riquelme and Anatoly Spitkovsky. Electron Injection by Whistler Waves in Non-relativistic Shocks. *Astrophys. J.*, 733:63, 2011. doi:10.1088/0004-637X/733/1/63.

Steven J Schwartz, Michelle F Thomsen, S J Bame, and John Stansberry. Electron heating and the potential jump across fast mode shocks. *J. Geophys. Res*, 93: 12923–12931, 1988. doi:10.1029/JA093iA11p12923.

J Scudder, A Mangeney, C Lacombe, C Harvey, C S Wu, and R R Anderson. The resolved layer of a collisionless, high beta, supercritical, quasi-perpendicular shock wave. III Vlasov Electrodynamics. *J. Geophys. Res*, 91:11075, January 1986a.

J D Scudder, T Aggson, T L Aggson, A Mangeney, C Lacombe, and C C Harvey. The resolved layer of a collisionless, high beta, supercritical, quasi-perpendicular shock wave. I - Rankine-Hugoniot geometry, currents, and stationarity. *J. Geophys. Res*, 91(A10):11019–11052, October 1986b. doi:10.1029/JA091iA10p11019.

V See, R F Cameron, and S J Schwartz. Non-adiabatic electron behaviour due to short-scale electric field structures at collisionless shock waves. *Annales Geophysicae*, 31(4):639–646, April 2013. doi:10.5194/angeo-31-639-2013.

M Thomsen, J Stansberry, S Bame, and J Gosling. Strong electron heating at the earth's bow shock. *J. Geophys. Res*, 92:10119–10124, January 1987.

Aaron Tran and Lorenzo Sironi. Electron Heating in Perpendicular Low-beta Shocks. *Astrophys. J.*, 900(2):L36, September 2020. ISSN 2041-8213. doi:10.3847/2041-8213/abb19c.

D Trotta and D Burgess. Electron acceleration at quasi-perpendicular shocks in sub- and supercritical regimes: 2D and 3D simulations. *Monthly Notices of the Royal Astronomical Society*, 482:1154–1162, 2019. doi:10.1093/mnras/sty2756.

I Y Vasko, F S Mozer, V V Krasnoselskikh, A V Artemyev, O V Agapitov, S D Bale, L Avanov, R Ergun, B Giles, P A Lindqvist, C T Russell, R Strangeway, and R Torbert. Solitary Waves Across Supercritical Quasi-Perpendicular Shocks. *Geophys. Res. Lett.*, 45(1):5809–5817, June 2018. doi:10.1029/2018GL077835.

I. Y. Vasko, F. S. Mozer, S. D. Bale, and A. V. Artemyev. Ion-Acoustic Waves in a Quasi-Perpendicular Earth's Bow Shock. *Geophys. Res. Lett.*, 49(11), June 2022. ISSN 0094-8276, 1944-8007. doi:10.1029/2022GL098640.

Ivan Y. Vasko, Rachel Wang, Forrest S. Mozer, Stuart D. Bale, and Anton V. Artemyev. On the Nature and Origin of Bipolar Electrostatic Structures in the Earth's Bow Shock. *Frontiers in Physics*, 8:156, June 2020. ISSN 2296-424X. doi:10.3389/fphy.2020.00156.

Jacco Vink. Supernova remnants: The X-ray perspective. *Astron. Astrophys. Rev.*, 20:49–120, 2012. doi:10.1007/s00159-011-0049-1.

Jacco Vink, Sjors Broersen, Andrei Bykov, and Stefano Gabici. On the electron-ion temperature ratio established by collisionless shocks. *Astronomy and Astrophysics*, 579:A13, 2015. doi:10.1051/0004-6361/201424612.

S Walker, H Alleyne, M Balikhin, M André, and T Horbury. Electric field scales at quasi-perpendicular shocks. *Annales Geophysicae*, 22(7):2291–2300, July 2004. doi:10.5194/angeo-22-2291-2004.

R Wang, I Y Vasko, F S Mozer, S D Bale, A V Artemyev, J W Bonnell, R Ergun, B Giles, P A Lindqvist, C T Russell, and R Strangeway. Electrostatic Turbulence and Debye-scale Structures in Collisionless Shocks. *Astrophys. J. Lett.*, 889(1):L9, January 2020. doi:10.3847/2041-8213/ab6582.

R. Wang, I. Y. Vasko, F. S. Mozer, S. D. Bale, I. V. Kuzichev, A. V. Artemyev, K. Steinvall, R. Ergun, B. Giles, Y. Khotyaintsev, P.-A. Lindqvist, C. T. Russell, and R. Strangeway. Electrostatic Solitary Waves in the Earth's Bow Shock: Nature, Properties, Lifetimes, and Origin. *J. Geophys. Res*, 126(7), July 2021. ISSN 2169-9380, 2169-9402. doi:10.1029/2021JA029357.

R. Wang, I. Y. Vasko, A. V. Artemyev, L. C. Holley, S. R. Kamaletdinov, A. Lotekar, and F. S. Mozer. Multisatellite Observations of Ion Holes in the Earth's Plasma Sheet. *Geophys. Res. Lett.*, 49(8), April 2022. ISSN 0094-8276, 1944-8007. doi:10.1029/2022GL097919.

L B Wilson, D G Sibeck, A W Breneman, O Le Contel, C Cully, D L Turner, V Angelopoulos, and D M Malaspina. Quantified energy dissipation rates in the terrestrial bow shock: 1. Analysis techniques and methodology. *J. Geophys. Res*, 119(8):6455–6474, August 2014. doi:10.1002/2014JA019929.

L B III Wilson, C A Cattell, P J Kellogg, K Goetz, K Kersten, J C Kasper, A Szabo, and M Wilber. Large-amplitude electrostatic waves observed at a supercritical interplanetary shock. *J. Geophys. Res*, 115(A):A12104, December 2010. doi:10.1029/2010JA015332.

L B Wilson III, D G Sibeck, A W Breneman, O Le Contel, C Cully, D L Turner, V Angelopoulos, and D M Malaspina. Quantified energy dissipation rates in the terrestrial bow shock: 2. Waves and dissipation. *J. Geophys. Res*, 119(8): 6475–6495, August 2014. doi:10.1002/2014JA019930.

C S Wu. A fast Fermi process - Energetic electrons accelerated by a nearly perpendicular bow shock. *J. Geophys. Res*, 89(A10):8857–8862, October 1984. doi:10.1029/JA089iA10p08857.

J R Wygant, M Bensadoun, and F S Mozer. Electric field measurements at subcritical, oblique bow shock crossings. *J. Geophys. Res*, 92:11109, October 1987. doi:10.1029/JA092iA10p11109.